Opto-Electronic Science

Supplementary information
May 2024, Vol. 3, No. 5

DOI: 10.29026/oes.2024.230046

Photo-driven fin field-effect transistor

Jintao Fu[1,2], Chongqian Leng[1], Rui Ma[1,3], Changbin Nie[1,2], Feiying Sun[1], Genglin Li[1,2] and Xingzhan Wei[1,2,3]*

[1]Chongqing Institute of Green and Intelligent Technology, Chinese Academy of Sciences, Chongqing 400714, China; [2]University of Chinese Academy of Sciences, Beijing 100049, China; [3]Chongqing School, University of Chinese Academy of Sciences, Chongqing 400714, China.
*Correspondence: XZ Wei, E-mail: weixingzhan@cigit.ac.cn

This file includes:

Section 1: Hall measurement result of PbS
Section 2: Dark transfer characteristic of the photo-FinFET
Section 3: Responsivity of the photo-FinFET under visible light
Section 4: Optical microscope image and photocurrent mapping of the photo-FinFET
Section 5: Infrared photoresponse of the photo-FinFET
Section 6: Response speed of the photo-FinFET under visible light
Section 7: Transient response of the photo-FinFET under infrared light
Section 8. Simulated electrostatic potential of the photo-FinFET
Section 9: Summary of silicon-based infrared photodetectors
Section 10: Characterization of the PbS film
Section 11: Fabrication process of the photo-FinFET

Supplementary information for this paper is available at https://doi.org/10.29026/oes.2024.230046

Open Access This article is licensed under a Creative Commons Attribution 4.0 International License.
To view a copy of this license, visit http://creativecommons.org/licenses/by/4.0/.
© The Author(s) 2024. Published by Institute of Optics and Electronics, Chinese Academy of Sciences.

Section 1: Hall measurement result of PbS

Table S1 | Hall measurement of PbS.

Annealing condition	Mobility ($cm^2 \cdot V^{-1} \cdot s^{-1}$)	Carrier concentration (cm^{-3})	Doping type
No annealing	10.67	3.21×10^{13}	p-type

Section 2: Dark transfer characteristic of the photo-FinFET

During the gate voltage modulation process, as the V_{bg} increases from 0 V to the positive value, the I_{ds} of the photo-FinFET initially experiences a slight decrease. This behavior can be attributed to the carrier transfer occurring at the interface between PbS and Si upon contact. The Fermi level disparity between PbS (p-type doping) and Si (n-type doping) drives this carrier transfer process. Specifically, upon contact, holes tend to transfer from PbS to Si, while electrons migrate from Si to PbS (as depicted in Fig. S1(a)). At this time, applying a positive V_{bg} to the Si channel can offset these additional holes and replenish the lost electrons due to the carrier transfer process. Throughout this progression, the initial increase in V_{bg} results in a reduction in hole concentration, leading to a slight decrease in I_{ds} (Fig. S1(b-d)). It is worth noting that the modulation effect of the V_{bg} on the Si channel is relatively weak, primarily due to the substantial thickness of the SiO_2 interlayer and the high resistivity of the bottom Si. Consequently, this slight decline in I_{ds} continues until V_{bg} reaches approximately 10 V, at which point I_{ds} begins to rise (Fig. 2(a)).

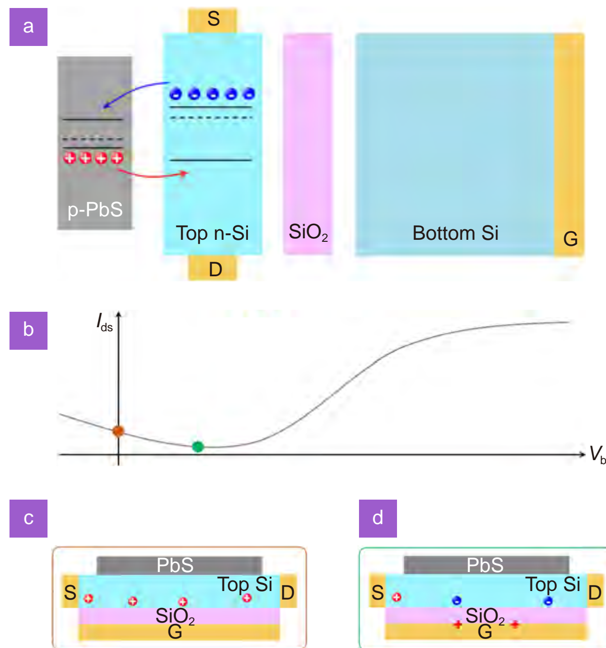

Fig. S1 | Illustration of the transfer characteristic of the photo-FinFET. (**a**) Schematic diagram of the charge transfer process upon contact between p-type doped PbS and n-type doped top Si. (b) Schematic diagram of the transfer characteristic curve of the photo-FinFET. (c, d) Schematic diagram of carrier states in Si channel. (c) and (d) correspond to the orange dot and green dot in (b), respectively.

Section 3: Responsivity of the photo-FinFET under visible light

It can be seen from Fig. S2 that as the V_{bg} increases positively, the responsivity of the photo-FinFET experiences a significant enhancement. This phenomenon can be attributed to the fact that a substantial positive V_{bg} can accumulate a considerable number of electrons within the Si channel, thereby amplifying the opening effect[S1]. In essence, when an increasing number of electrons accumulate in the Si channel, the photo-FinFET can achieve a larger conduction current once the photovoltage opens the Si channel by compressing the depletion region. However, it is crucial to mention that as the electron concentration continues to rise, the photo-FinFET will eventually reach a saturation state. As a result, further increases in the V_{bg} will no longer yield more photocurrent. Furthermore, the introduction of numerous carriers caused by the large V_{bg}, via capacitive coupling, can bring higher levels of noise, ultimately diminishing the sensitivity of the photo-FinFET.

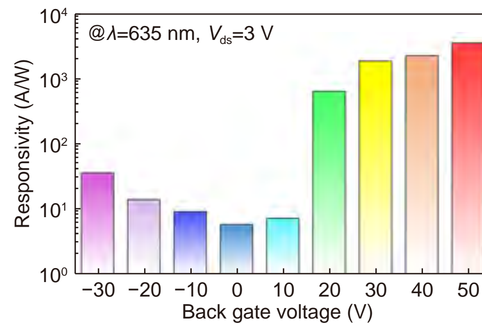

Fig. S2 | Responsivity of the photo-FinFET in response to 635 nm illumination under different V_{bg}.

Section 4: Optical microscope image and photocurrent mapping of the photo-FinFET

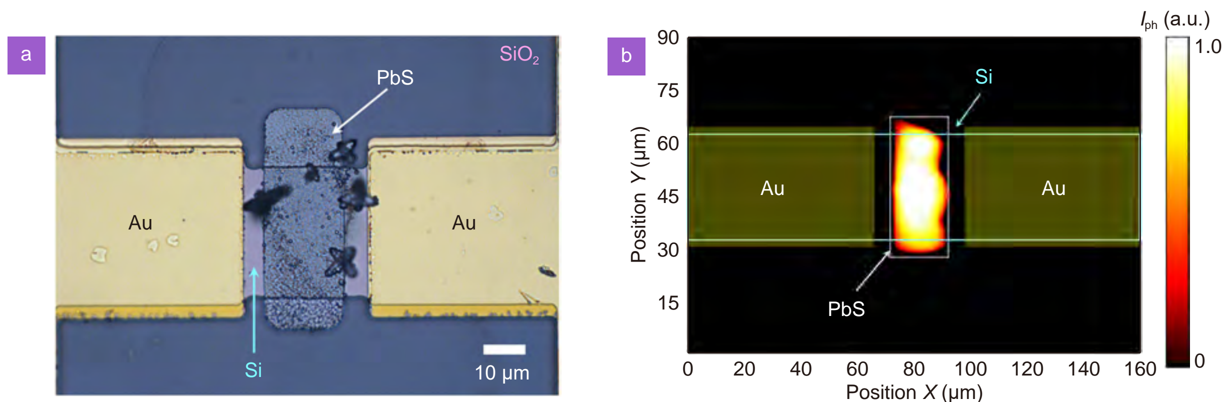

Fig. S3 | Characterization of the photo-FinFET. (**a**) Optical microscope image of the photo-FinFET, in which the PbS film wraps the Si channel. (**b**) Photocurrent mapping result of the photo-FinFET. A 1550 nm laser was used to excite carriers. The light blue, yellow, and white boxes represent Si channel, electrode, and PbS areas, respectively.

Section 5: Infrared photoresponse of the photo-FinFET

According to Fig. S4(c) and S4(d), it can be seen that the infrared photoresponse of the photo-FinFET increases with the increase of the V_{bg}. To elucidate this phenomenon, the net electron density of the photo-FinFET under varying V_{bg} was simulated (Fig. S5). The net electron density is derived by subtracting the electron density in the dark state from the electron concentration in the light state. As depicted in Fig. S5, an increase in V_{bg} leads to a continuous rise in the net electron density within the Si channel. A higher net electron density implies a more substantial photocurrent output, aligning with the observed experimental phenomenon. However, the impact of enhancing the photocurrent by elevating the V_{bg} has limitations. Figure S5(b) illustrates that as the V_{bg} increases from 0 V, the net electron density initially experiences a significant boost. Nevertheless, as the V_{bg} continues to increase, the effect of increasing the net electron density (infrared photoresponse) by applying a large gate voltage reaches saturation. At this point, the V_{bg} is set to 50 V, which corresponds to the maximum gate voltage applied during the experiments.

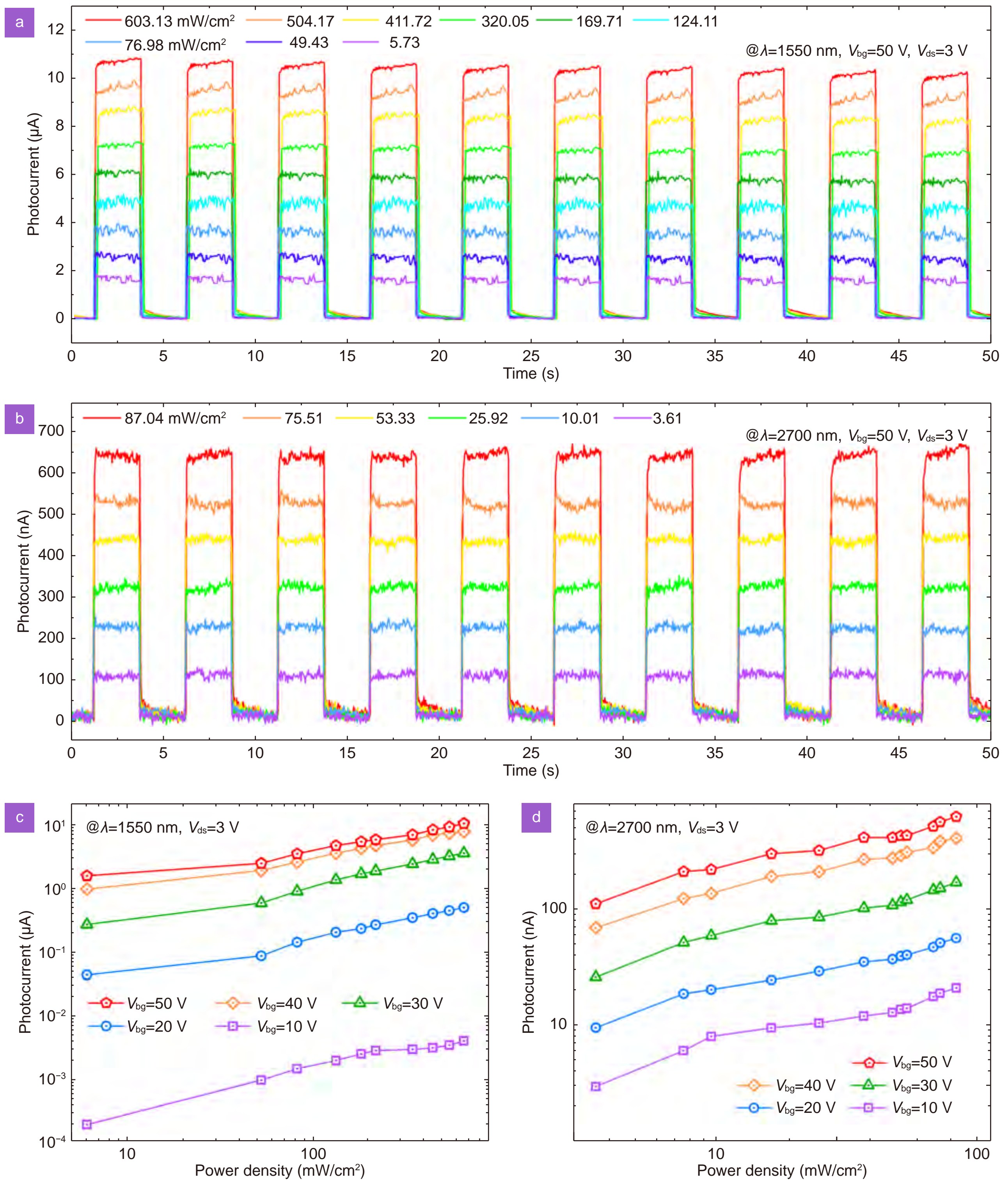

Fig. S4 | Photoresponse of the photo-FinFET under infrared illumination. (**a**, **b**) *I-T* curves of the photo-FinFET under 1550 nm and 2700 nm illumination, respectively. (**c**, **d**) Photocurrent of the photo-FinFET as a function of light power density under different V_{bg}.

Moreover, Fig. S5(b) indicates that, besides increasing the net electron density on the SiO_2 side of the Si channel, the V_{bg} also slightly decreases the net electron density in certain areas inside the Si channel. This phenomenon is related to the electron accumulation induced by the gate voltage. In specific, the electron accumulation originates from electron injection from the source electrode, spontaneous thermal excitation of carriers in the semiconductor, and the attraction of existing electrons in the channel. Among them, the attraction of existing electrons in the channel results in a slight re-

duction in the net electron concentration in certain areas inside the Si channel. These accumulated electrons can also shield the influence of the V_{bg}, causing the net electron density near the PbS-Si heterojunction to undergo slight or nearly negligible changes.

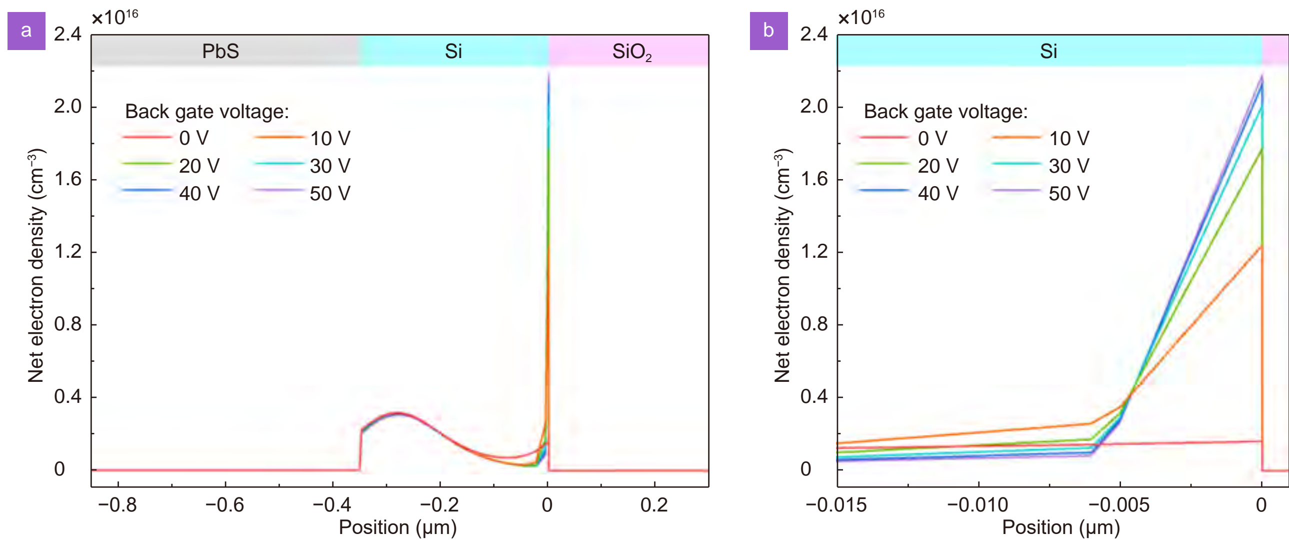

Fig. S5 | Net electron density in the photo-FinFET under 1550 nm illumination. (**a**) Simulated net electron density distribution perpendicular to the Si channel inside the photo-FinFET under different back gate voltages. The net electron density is calculated by subtracting electron density in the dark from electron density under illumination, representing the change in electron density induced by infrared light. (**b**) Enlarged net electron density distribution in the top Si channel region. As back gate voltage increases, the net electron density first increases rapidly, and then the increment tends to saturation.

Section 6: Response speed of the photo-FinFET under visible light

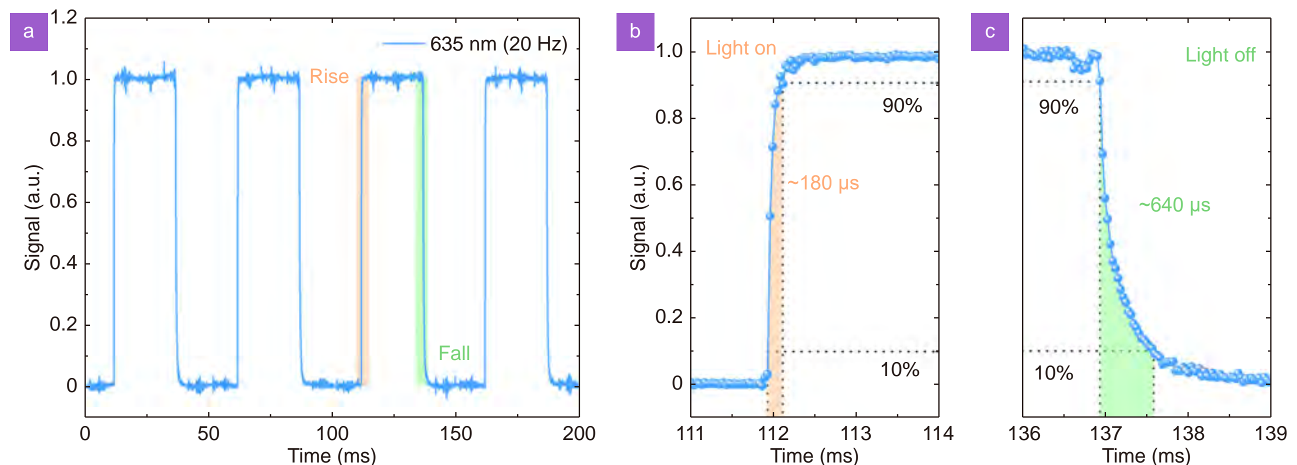

Fig. S6 | Transient response of the photo-FinFET under 635 nm illumination. (**a**) Output signal of the photo-FinFET in response to 635 nm light with a modulation frequency of 20 Hz. (**b**, **c**) Enlarged views of the rising and falling edges (indicated by the shaded boxed regions in (a)). The rising edge (or falling edge) is defined as the time required for the signal to rise from 10% to 90% of its peak value (or decline from 90% to 10% of its peak value).

Section 7: Transient response of the photo-FinFET under infrared light

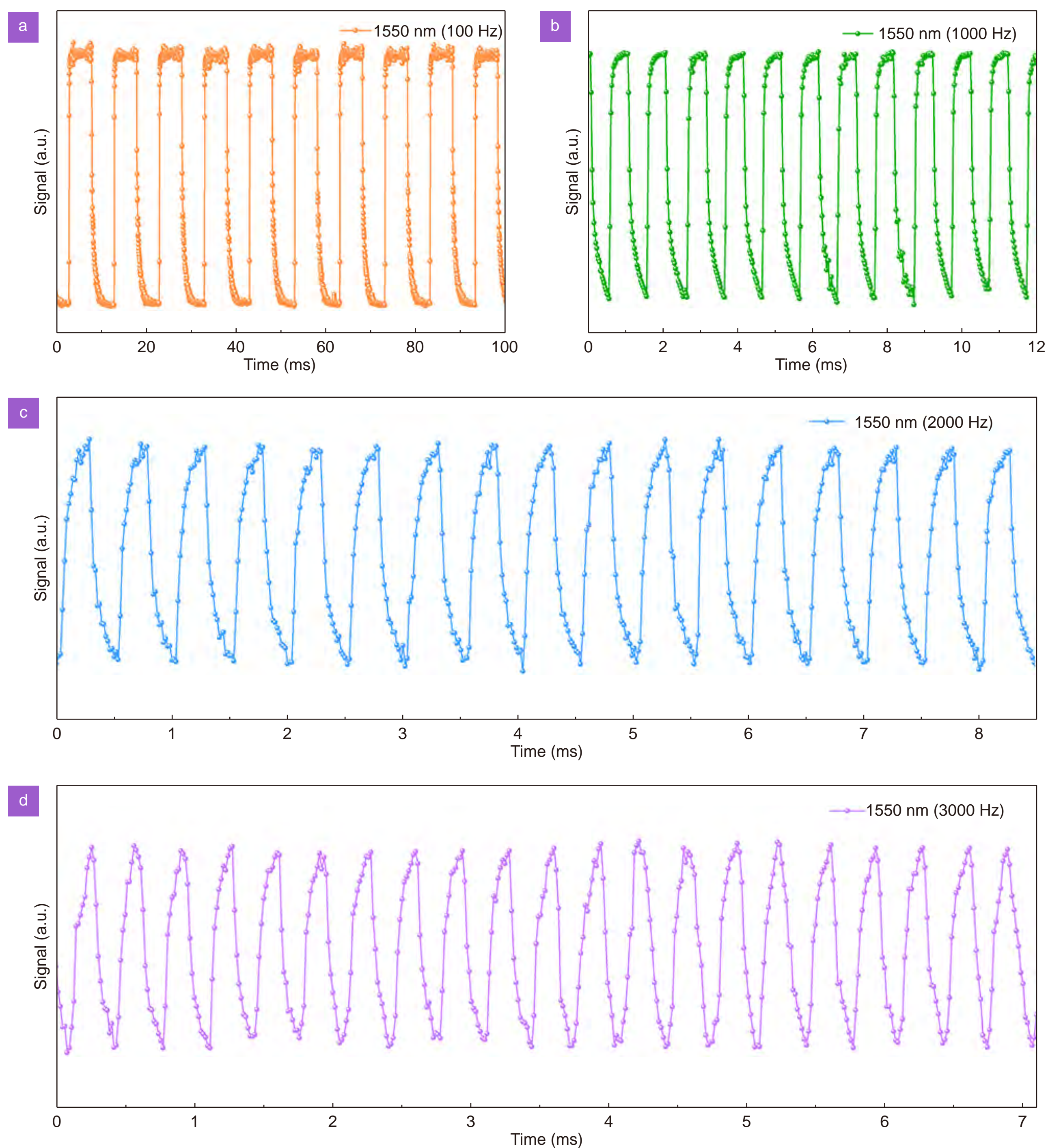

Fig. S7 | Transient response of the photo-FinFET under 1550 nm illumination with different modulation frequencies. The modulation frequencies of the 1550 nm laser are (**a**) 100 Hz, (**b**) 1000 Hz, (**c**) 2000 Hz, and (**d**) 3000 Hz, respectively.

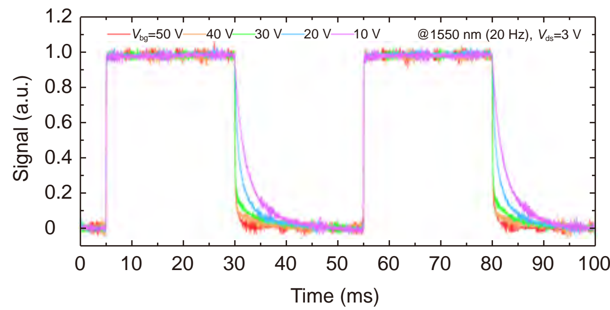

Fig. S8 | Infrared response speed of the photo-FinFET under different V_{bg}.

Section 8: Simulated electrostatic potential of the photo-FinFET

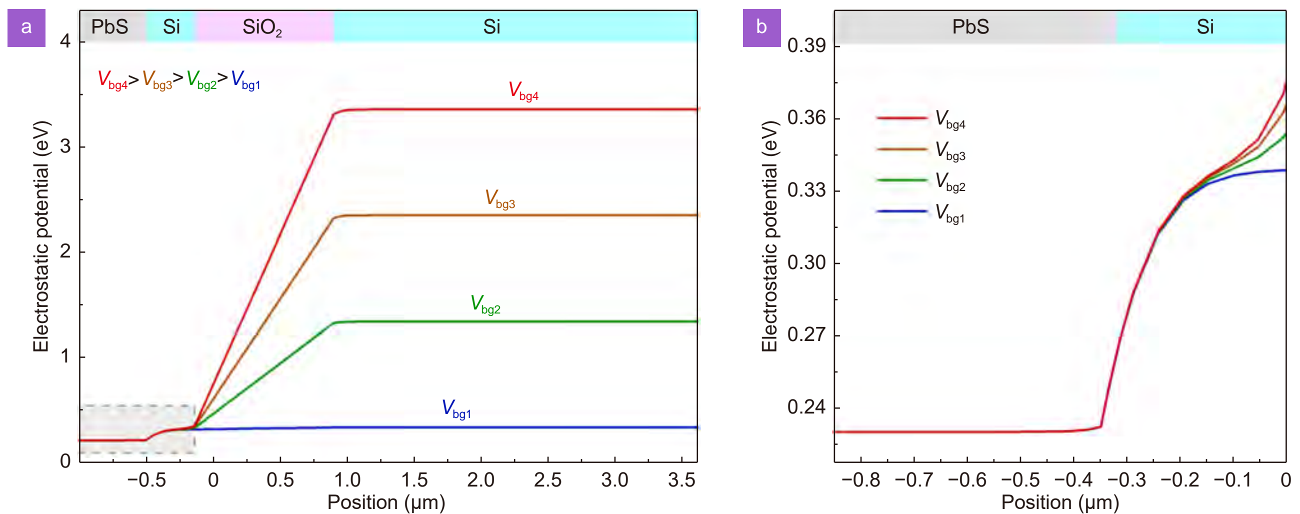

Fig. S9 | Electrostatic potential in the photo-FinFET. (**a**) Simulated electrostatic potential distribution perpendicular to the Si channel inside the photo-FinFET under various back gate voltages. (**b**) A magnified view from the gray area in (a). The values of V_{bg1}, V_{bg2}, V_{bg3}, and V_{bg4} are 0 V, 1 V, 2 V, and 3 V, respectively. As V_{bg} increases, significant electrostatic potential changes occur in the buried oxide layer due to the accumulation of equal numbers of electrons and holes in the top Si and bottom Si, respectively. In addition, the accumulated electrons in the top Si near the buried oxide layer effectively shield the electric field from the back gate electrode. Therefore, the electrostatic potential of the PbS-Si junction region exhibits negligible changes under varying V_{bg}.

Section 9: Summary of silicon-based infrared photodetectors

Up to now, various strategies have been explored to enable Si-based infrared photodetection. These strategies mainly encompass integrating infrared-absorbing material, manufacturing black Si, utilizing the internal photoemission effect, and hyper-doping Si.

(i) Integrating infrared-absorbing materials: This approach involves integrating classical infrared-sensitive materials, such as Ge, III-V semiconductors, and HgCdTe, with Si through epitaxy[S2–S4]. Moreover, emerging infrared-absorbing materials, including PbS CQDs[S5,S6] and HgTe CQDs[S7], can also be incorporated into Si using techniques like printing or spin-coating.

(ii) Utilizing the internal photoemission effect: The internal photoemission effect generally occurs at the interface of the metal-semiconductor Schottky junction. When a metal absorbs infrared light, photoexcited hot carriers can cross the Schottky barrier into the semiconductor, generating a photocurrent. This process enables the sensing of infrared light with photon energy smaller than the semiconductor bandgap but larger than the Schottky barrier[S8].

(iii) Manufacturing black Si: By treating the Si surface with laser or chemical etching, a light-trapping structure known as black Si can be created[S9]. Compared with regular Si, black silicon has greatly enhanced light absorption capability in the near-infrared range.

(iv) Hyper-doping Si: Hyper-doping involves introducing excess impurity atoms into Si[S10], promoting the sub-bandgap absorption of Si and broadening its light absorption range.

Table S2 | Performance summary of Si-based photodetectors.

Strategy	Structure	Wavelength (nm)	Responsivity (A/W)	Specific detectivity ($cm\cdot Hz^{1/2}\cdot W^{-1}$)	NEP ($W/Hz^{1/2}$)	Response speed	Ref
Integrating infrared-absorbing materials	Si: PbS CQDs	1540	0.264	1.47×10^{11}	2.89×10^{-12}	τ_{rise} = 2.04 μs τ_{fall} = 5.34 μs	ref.[S11]
	Si: PbS CQDs	1230	0.4	5×10^{10}	-	-	ref.[S12]
	PbS CQDs: Si	1300	1×10^{4}	1.8×10^{12}	-	τ_{rise} = 10 μs τ_{fall} = 10 μs	ref.[S13]
	Si+GeSn	2000	0.093	-	-	-	ref.[S14]
Utilizing the internal photoemission effect	Gra+Si (Optical cavity)	1550.5	0.02	5.1×10^{7}	3.5×10^{-10}	12 GHz (Theory)	ref.[S15]
	Gra+Si (Waveguide)	1550	0.085	-	1.1×10^{-12}	-	ref.[S16]
	Gra-Si	2000	1.6×10^{-4}		1.31×10^{-10}	-	ref.[S17]
	Si+metal plasma	1375	1	1.63×10^{8}	9.23×10^{-12}	-	ref.[S18]
Manufacturing black Si	Black Si	1319	5.53×10^{-4}	3.4×10^{7}	9.4×10^{-7}	-	ref.[S19]
		1550	4.58×10^{-4}	2.8×10^{7}	1.1×10^{-6}		
	Black Si	1080	497	1.22×10^{14}	-	τ_{rise} = 0.65 ms τ_{fall} = 2.13 ms	ref.[S20]
		1310	0.58	-			
	Black Si	1030	0.367	-	-	τ_{rise} = 53 ms τ_{fall} = 64 ms	ref.[S21]
	Black Si	955	0.7	6.3×10^{13}		τ_{rise} = 51 μs τ_{fall} = 318 μs	ref.[S22]
Hyper-doping Si	Te-Si	1200	0.002	1.1×10^{9}	9×10^{-9}	4.2 kHz	ref. [S10]
		1550	3×10^{-4}	3×10^{7}	2×10^{-8}		
Light absorption dominated by Si	Gra+SOI	532	1.4×10^{4}	1.61×10^{13}	-	80 kHz	ref. [S1]
	MoS_2+Si	808	0.3	1×10^{13}	-	τ_{rise} = 3 μs τ_{fall} = 40 μs	ref.[S23]
	Gra+Si	488	0.225	7.69×10^{9}	9.2×10^{-13}	τ_{rise} = 1.2 ms τ_{fall} = 3 ms	ref.[S24]
	Gra+Si (Pt nanoparticles)	532	26	7.5×10^{10}	4.2×10^{-12}	78 ns	ref.[S25]
	$AgInTe_2$-Si	980	2.82	8.12×10^{11}	2.46×10^{-13}	τ_{rise} = 5.2 μs τ_{fall} = 18.4 μs	ref.[S26]
Photo-driven fin field-effect transistor	PbS-SOI	635	1961	1.8×10^{11}	1.3×10^{-14}	τ_{rise} = 180 μs τ_{fall} = 640 μs	This work
		1550	45.2	7.7×10^{8}	3.2×10^{-12}	τ_{rise} = 150 μs τ_{fall} = 490 μs	
		2700	5	1.1×10^{8}	2.3×10^{-11}	-	

Supplementary Note: Difference in responsivity under visible and infrared light

The photo-FinFET showcases higher responsivity under visible light (635 nm) than under infrared light (1550 nm and 2700 nm). This outcome can be attributed to the fact that both Si and PbS exhibit light absorption in the visible light spectrum. In contrast, under infrared illumination with photon energy below the bandgap of Si, only PbS absorbs infrared light and generates free carriers.

Additionally, the metal-Si Schottky junction undergoes shrinkage after Si absorbs visible light. This process resembles the compression of the space charge region in a photodiode or solar cell, which is caused by the open-circuit voltage under illumination[S27]. Consequently, upon visible light irradiation, alterations occur not only in the PbS-Si heterojunction but also in the metal-Si Schottky junctions on both sides of the Si channel. This leads to a reduction in con-

tact resistance, enhancing the efficiency of the electrode in collecting photocurrent. In contrast, infrared irradiation exclusively affects the state of the PbS-Si heterojunction. Therefore, the photo-FinFET exhibits stronger responsivity under visible light compared to infrared light.

Supplementary Note: Infrared responsivity of the photo-FinFET

The discrepancy in the responsivity of the photo-FinFET under 2700 nm illumination compared to 1550 nm illumination can be attributed to the interplay between the thickness of the infrared photosensitive layer and the penetration depth of infrared light at different wavelengths. As the wavelength of light increases, the penetration depth of light into semiconductor materials deepens. Generally, without specialized optical structures, the penetration depth of 1550 nm light is smaller than that of 2700 nm light. In the photo-FinFET, the PbS infrared photosensitive gate has a thickness of approximately 500 nm (Fig. S10). While this limited thickness allows the PbS gate to effectively absorb 1550 nm light, the PbS gate fails to fully utilize 2700 nm light. Therefore, the responsivity of the photo-FinFET is higher under 1550 nm light than under 2700 nm light.

While enhancing light absorption at 2700 nm is achievable by increasing the thickness of the PbS infrared photosensitive gate, it is crucial to note that a thicker photosensitive layer also extends the transport distance of infrared photogenerated carriers. Throughout this transport process, the unavoidable recombination of photogenerated carriers poses a challenge to the infrared photodetection capability of the detector[S28,S29].

Supplementary Note: Performance of the photo-FinFET at varying V_{bg}

Although a low V_{bg} results in low noise, which is appealing for achieving a low NEP, the responsivity also decreases with the reduction of V_{bg}. The NEPs of the photo-FinFET at V_{bg} = 10 V and 20 V are 1.4×10^{-10} W·Hz$^{-1/2}$ and 4.9×10^{-11} W·Hz$^{-1/2}$ (@ λ = 2700 nm), respectively, and they are higher than the NEP of the photo-FET at V_{bg} = 30 V. This discrepancy is attributed to the increased responsivity at high gate voltages.

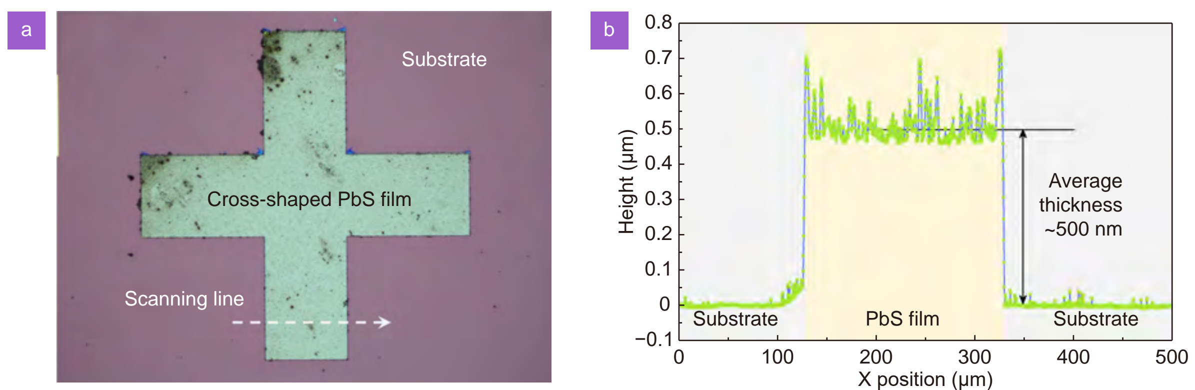

Fig. S10 | Thickness characteristic for the PbS film. (**a**) Optical microscope image of the cross-shaped PbS film. (**b**) Height profile of the PbS film along the scanning line in (a). The thickness of the PbS film was measured by a step profiler. The growth batch of the cross-shaped PbS film and the PbS film in the photo-FinFET are the same.

Section 10: Characterization of the PbS film

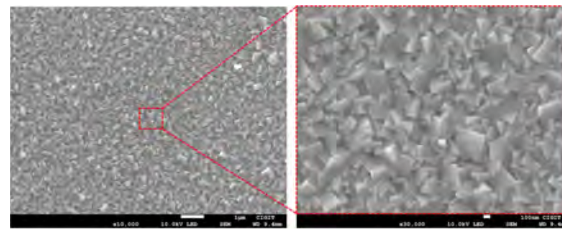

Fig. S11 | Scanning electron microscope (SEM) images of the PbS film. The square geometry presented by the PbS crystal is consistent with its intrinsic cubic crystal structure. The PbS film is dense and continuous, completely covering the substrate.

Section 11: Fabrication process of the photo-FinFET

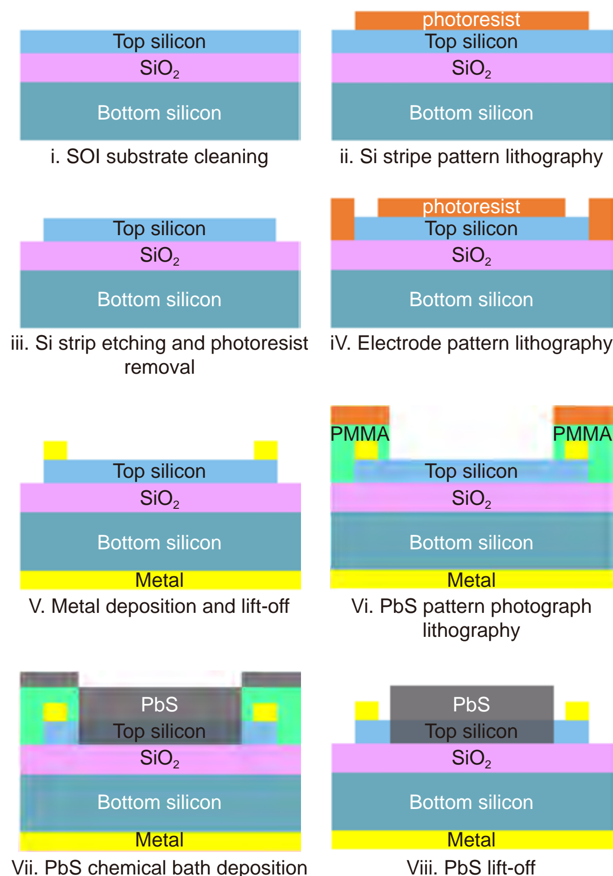

Fig. S12 | Schematic diagram of the fabrication process of the photo-FinFET.

Table S3 | Parameters of the SOI substrate.

Layer	Thickness (μm)	Doping condition	Resistivity (Ω·cm)
Top Si	0.35	n-type	1-10
Buried SiO_2	1	-	(insulation)
Bottom Si	500	n-type	1-10

Supplementary Note: Metal-Si Schottky junction

In the photo-FinFET, the direct contact between the metal electrode and Si channel forms a Schottky junction. The Schottky junction increases the contact resistance between metal and Si, which affects the efficiency of the electrode in collecting charges. Nevertheless, the metal-Si Schottky junction imposes negligible impact on the state of the PbS-Si heterojunction.

In specific, the electrode of the photo-FinFET features a layer of Cr between Au and Si (refer to the Method section

for details). The work function of Cr is approximately 4.6 eV. The Si channel is n-type doped, exhibiting a resistivity within the range of 1–10 Ω·cm. Based on this resistivity, a rough estimation of the doping concentration (N_d) in the Si channel falls between 4×10^{14} cm^{-3} and 6×10^{15} cm^{-3} [S27]. Assuming complete ionization of all dopants, the relationship between the Fermi level (E_F) and the free carrier concentration (n_0) can be expressed by Eq. (S1):

$$n_0 = N_c \exp\left[\frac{-(E_c - E_F)}{k_B T}\right] , \tag{S1}$$

where N_c is the effective density of states in the conduction band (2.8×10^{19} cm^{-3} for Si), E_c is the conduction band, k_B is the Boltzmann constant, and T is the temperature. The difference between the Fermi level and the conduction band in Si can be calculated as 0.29–0.22 eV.

According to the metal-semiconductor Schottky junction model, the Schottky barrier height (φ_{SBH}) can be calculated by using Eq. (S2):

$$\varphi_{SBH} = \varphi_m - \chi , \tag{S2}$$

where φ_m is the metal work function (4.6 eV for Cr) and χ is the semiconductor affinity (4.05 eV for Si). The calculated φ_{SBH} is 0.55 eV.

Based on the Schottky barrier height, the built-in electric field (V_{bi}) of the Schottky junction can be obtained according to Eq. (S3):

$$V_{bi} = \frac{\varphi_{SBH} - \varphi_n}{q} , \tag{S3}$$

where q is the element charge and φ_n is the difference between the Fermi level and the conduction band (that is $E_c - E_F$). Based on the previous results, V_{bi} can be calculated to be 0.26–0.33 V.

For a Schottky junction, the relationship between the depletion region width (W_{dep}) and V_{bi} in the semiconductor is as follows:

$$W_{dep} = \left[\frac{2\varepsilon_0 \varepsilon_{Si} (V_{bi} + V_R)}{qN_d}\right]^{1/2} , \tag{S4}$$

where, ε_0 is the permittivity, ε_{Si} is the relative permittivity of Si (11.7), V_R is the reverse bias voltage (0 V), and N_d is the doping concentration. By exploiting V_{bi}, W_{dep} of the metal-Si Schottky junction can be obtained to be 0.92–0.27 μm.

Based on the preceding discussion, it can be seen that the width of the metal-Si depletion region does not extend into the PbS-Si heterojunction region. The microscopic image of the photo-FinFET (Fig. S3) reveals that the electrode area is approximately 5 μm away from the PbS region. Consequently, in the photo-FinFET, the Schottky junction formed by the metal electrode and Si channel primarily affects the efficiency of charge collection, without influencing the state of the PbS-Si heterojunction.

References

S1. Fu JT, Nie CB, Sun FY et al. Photo‐driven semimetal–semiconductor field‐effect transistors. *Adv Opt Mater* **11**, 2201983 (2023).

S2. Michel J, Liu JF, Kimerling LC. High-performance Ge-on-Si photodetectors. *Nat Photonics* **4**, 527–534 (2010).

S3. Kay R, Bean R, Zanio K et al. HgCdTe photovoltaic detectors on si substrates. *Appl Phys Lett* **51**, 2211–2212 (1987).

S4. Jia BW, Tan KH, Loke WK et al. Monolithic integration of InSb photodetector on silicon for mid-infrared silicon photonics. *ACS Photonics* **5**, 1512–1520 (2018).

S5. Liu J, Liu PL, Chen D et al. A near-infrared colloidal quantum dot imager with monolithically integrated readout circuitry. *Nat Electronics* **5**, 443–451 (2022).

S6. Zhou W, Zheng L, Ning ZJ et al. Silicon: quantum dot photovoltage triodes. *Nat Commun* **12**, 6696 (2021).

S7. Tang X, Chen ML, Kamath A et al. Colloidal quantum-dots/graphene/silicon dual-channel detection of visible light and short-wave infrared. *ACS Photonics* **7**, 1117–1121 (2020).

S8. Scales C, Berini P. Thin-film schottky barrier photodetector models. *IEEE J Quantum Electron* **46**, 633–643 (2010).

S9. Branz HM, Yost VE, Ward S et al. Nanostructured black silicon and the optical reflectance of graded-density surfaces. *Appl Phys Lett* **94**, 231121 (2009).

S10. Wang M, García‐Hemme E, Berencén Y et al. Silicon‐based intermediate‐band infrared photodetector realized by Te hyperdoping. *Adv Opt Mater* **9**, 2001546 (2021).

S11. Xu KM, Xiao XB, Zhou WJ et al. Inverted Si: PbS colloidal quantum dot heterojunction-based infrared photodetector. *ACS Appl Mater Inter-*

faces **12**, 15414–15421 (2020).

S12. Masala S, Adinolfi V, Sun JP et al. The silicon: colloidal quantum dot heterojunction. *Adv Mater* **27**, 7445–7450 (2015).

S13. Adinolfi V, Sargent EH. Photovoltage field-effect transistors. *Nature* **542**, 324–327 (2017).

S14. Cong H, Xue CL, Zheng J et al. Silicon based GeSn p-i-n photodetector for SWIR detection. *IEEE Photonics J* **8**, 6804706 (2016).

S15. Casalino M, Sassi U, Goykhman I et al. Vertically illuminated, resonant cavity enhanced, graphene-silicon schottky photodetectors. *ACS Nano* **11**, 10955–10963 (2017).

S16. Goykhman I, Sassi U, Desiatov B et al. On-chip integrated, silicon-graphene plasmonic schottky photodetector with high responsivity and avalanche photogain. *Nano Lett* **16**, 3005–3013 (2016).

S17. Casalino M, Russo R, Russo C et al. Free-space schottky graphene/silicon photodetectors operating at 2 μm. *ACS Photonics* **5**, 4577–4585 (2018).

S18. Tanzid M, Ahmadivand A, Zhang R et al. Combining plasmonic hot carrier generation with free carrier absorption for high-performance near-infrared silicon-based photodetection. *ACS Photonics* **5**, 3472–3477 (2018).

S19. Hu F, Dai XY, Zhou ZQ et al. Black silicon Schottky photodetector in sub-bandgap near-infrared regime. *Opt Express* **27**, 3161–3168 (2019).

S20. Huang S, Wu Q, Jia ZX et al. Black silicon photodetector with excellent comprehensive properties by rapid thermal annealing and hydrogenated surface passivation. *Adv Opt Mater* **8**, 1901808 (2020).

S21. Zhao XN, Lin K, Zhao B et al. Broadband MSM photodetector based on S-doped black silicon fabricated by femtosecond laser. *Appl Surf Sci* **619**, 156624 (2023).

S22. Zhang YB, Loh JYY, Kherani NP. Facilely achieved self-biased black silicon heterojunction photodiode with broadband quantum efficiency approaching 100%. *Adv Sci (Weinh)* **9**, 2203234 (2022).

S23. Wang L, Jie JS, Shao ZB et al. MoS_2/Si heterojunction with vertically standing layered structure for ultrafast, high-detectivity, self-driven visible-near infrared photodetectors. *Adv Funct Mater* **25**, 2910–2919 (2015).

S24. An XH, Liu FZ, Jung YJ et al. Tunable graphene-silicon heterojunctions for ultrasensitive photodetection. *Nano Lett* **13**, 909–916 (2013).

S25. Huang K, Yan YC, Li K et al. High and fast response of a graphene-silicon photodetector coupled with 2D fractal platinum nanoparticles. *Adv Opt Mater* **6**, 1700793 (2018).

S26. You S, Zhang L, Yu YQ et al. Nanoscale $AgInTe_2$/Si truncated quasitetrahedrons for heterostructured photodetectors. *ACS Appl Nano Mater* **4**, 5785–5795 (2021).

S27. Neamen D. *Semiconductor Physics and Devices* 3rd ed (McGraw-Hill, Inc. , 2002).

S28. Nikitskiy I, Goossens S, Kufer D et al. Integrating an electrically active colloidal quantum dot photodiode with a graphene phototransistor. *Nat Commun* **7**, 11954 (2016).

S29. Ni ZY, Ma LL, Du SC et al. Plasmonic silicon quantum dots enabled high-sensitivity ultrabroadband photodetection of graphene-based hybrid phototransistors. *ACS Nano* **11**, 9854–9862 (2017).